Dynamics of Future Soil Moisture Drought in Southwest North America: Linkages across Seasons in the Ocean–Atmosphere–Land System

Richard Seager,[a] Mingfang Ting,[a,b] Patrick Alexander,[a] Haibo Liu,[a] Cuihua Li,[a]
and Jennifer Nakamura[a]

[a] *Lamont Doherty Earth Observatory of Columbia University, Palisades, New York*
[b] *Columbia Climate School, Columbia University in the City of New York, New York, New York*

(Manuscript received 10 May 2024, in final form 8 January 2025, accepted 3 February 2025)

ABSTRACT: Southwest North America is projected by models to aridify, defined as declining summer soil moisture, under the influence of rising greenhouse gases. Here, we investigate the driving mechanisms of aridification that connect the oceans, atmosphere, and land surface across seasons. The analysis is based on atmosphere model simulations forced by imposed sea surface temperatures (SSTs). For the historical period, these are the observed ones, and the model is run to 2041 using SSTs that account for realistic and plausible evolutions of Pacific Ocean and Atlantic Ocean interannual to decadal variability imposed on estimates of radiatively forced SST change. The results emphasize the importance of changes in precipitation throughout the year for declines in summer soil moisture. In the worst-case scenario, a cool tropical Pacific and warm North Atlantic lead to reduced cool season precipitation and soil moisture. Drier soils then persist into summer such that evapotranspiration reduces and soil moisture partially recovers. In the best-case scenario, the opposite states of the oceans lead to increased cool season precipitation but higher evapotranspiration prevents this from increasing summer soil moisture. Across the scenarios, atmospheric humidity is primarily controlled by soil moisture: drier soils lead to reduced evapotranspiration, lower air humidity, and higher vapor pressure deficit (VPD). Radiatively forced change reduces fall precipitation via anomalous transient eddy moisture flux divergence. Fall drying causes soils to enter winter dry such that, even in the best-case scenario of cool season precipitation increase, soil moisture remains dry. Radiative forcing reduces summer precipitation aided by reduced evapotranspiration from drier soils.

SIGNIFICANCE STATEMENT: Southwest North America has long been projected to undergo aridification under rising greenhouse gases. In this model-based paper, we examine how coupling across seasons between the atmosphere and land system moves the region toward reduced summer soil moisture. The results show the dominant control on summer soil moisture by precipitation throughout the year. It also shows that even in best-case scenarios when changes in decadal modes of ocean variability lead to increases in cool season precipitation, rising spring and summer evapotranspiration means this does not translate into increased summer soil moisture. The work places projections of regional aridification on a firmer basis of understanding of the ocean driving of the atmosphere and its coupling to the land system.

KEYWORDS: North America; Drought; Soil moisture; General circulation models; Decadal variability;
Pacific decadal oscillation

1. Introduction

As the atmosphere warms, it can hold more moisture according to the exponential relation between saturation humidity and temperature described by the Clausius–Clapeyron relation. Potential evapotranspiration (PET) is a theoretical quantity that measures how much water could evaporate from a well-watered crop given the environmental conditions of radiation, winds, and air temperature. Given the dependence of saturation humidity on temperature, and all else equal, PET increases with temperature under global warming, governed by an increase in vapor pressure deficit (VPD), the difference between saturation vapor pressure, and actual vapor pressure. Indeed, Scheff and Frierson (2014) show PET increase under global warming in climate models is driven almost entirely by the effect of a warming atmosphere. Consequently, by a variety of metrics of aridity, such as the aridity index, AI = P/PET, where P is the precipitation; the Palmer drought severity index (PDSI); or the standardized precipitation evapotranspiration index, global climate models project widespread continental drying over the coming century (Cook et al. 2014; Lickley and Solomon 2018; Greve et al. 2019; Scheff and Frierson 2015; Vicente-Serrano et al. 2022). Only in places where precipitation increases a lot is the drying influence of warming overwhelmed. Of course, the use of such metrics has been greatly criticized recently because of their means of computation of PET (e.g., Milly and Dunne 2011, 2016). Indeed, patterns of actual soil moisture (sm) drying are less expansive than those of aridity increase from simple metrics (e.g., Berg et al. 2017; Greve et al. 2019; Cook et al. 2020). However, summer sm declines under increased CO_2 in an actual climate model with realistic geography were in fact first noted by Manabe et al. (1981). Summer sm is of critical importance given its direct relevance to agriculture

---

Corresponding author: Richard Seager, seager@ldeo.columbia.edu

DOI: 10.1175/JCLI-D-24-0235.1

and as a proxy for water availability during the summer season of enhanced need for water across human systems. Cook et al. (2015) show that the drying in PDSI is quite predictive of actual declines in summer sm in state-of-the-art climate models in the North American Southwest and Great Plains. This is likely due to PDSI allowing actual evapotranspiration (ET) to drop below PET when soil moisture is limited. Despite this drying, by aridity metrics or sm, vegetation health in climate models, as measured by the gross primary productivity or the leaf area index, actually increases in many supposedly more arid regions as a result of the ecophysiological influence of rising CO_2 on plants (e.g., Swann et al. 2016; Mankin et al. 2017, 2018, 2019; Berg and McColl 2021).

But how does this adjustment in the land–atmosphere system occur? Naively, one might think that enhanced VPD and PET would reduce sm by increased ET. In essence, this would be a migration of moisture from the land surface into the atmosphere. In regions that are not water limited, that does seem to occur and summer VPD and ET increase together, whereas, in more water-limited regions, while VPD increases in summer, ET actually decreases (e.g., Cook et al. 2014). Southwest North America (SWNA) is one such region (see also Mankin et al. 2017). In these regions, how is it that summer sm declines given that reduced summer ET is acting to increase the sm despite increased demand from the atmosphere (VPD)? This must be explained by some connectivity across seasons in the land–atmosphere system. It could be that summer sm inherits low sm from spring. Spring sm could, in turn, be low due to either high ET or low P. For example, in an analysis of modeled decreases in summer sm in Europe, Tuel and Eltahir (2021) identified the importance of winter P reduction in setting up summer sm decreases in the south.

SWNA is a region currently undergoing major climate stress that has been enduring a megadrought for the entire twenty-first century so far (Williams et al. 2020, 2022). While atmosphere modeling work has shown that the current megadrought is largely driven by presumably natural sea surface temperature (SST) variations which forced cool season precipitation reduction (Lehner et al. 2020; Seager et al. 2023), further drying is projected due to a combination of changing precipitation patterns and rising temperatures (Maloney et al. 2014; Cook et al. 2015). Seager et al. (2023) projected the future out to 2041 using an SST-forced atmosphere model subject to plausible scenarios for the Pacific decadal oscillation (PDO; Newman et al. 2016) and the Atlantic multidecadal oscillation (AMO; Kushnir 1994) and radiatively forced SST change. In the best-case scenario for the 2030s decade (a warm tropic phase of the PDO and a cool state of the AMO), forced change means summer sm is wetter than it is during the current megadrought but not as wet as in the late twentieth century pluvial of the 1980s and 1990s. In the worst-case scenario (the opposite signed anomalies for the PDO and AMO), summer soils are even drier than they have been in the twenty-first century megadrought. If, under further radiative forcing, SST change continues the pattern of no warming in the equatorial Pacific cold tongue, in contrast to climate model projections of cold tongue warming [see Lee et al. (2022) for a review of evidence and mechanisms for tropical Pacific SST trends], then drying is exacerbated by a stronger drop in cool season precipitation.

The Seager et al. (2023) model simulations focused on the ocean forcing of teleconnections and how these impact P, $P - \mathrm{ET}$, and sm. Here, we exploit these same model simulations to study the cross-season connections in the atmosphere–land system that establish new and more arid conditions in SWNA with changing balances between P, ET, and sm. We will examine how relations between P, ET, sm, air humidity, and VPD are established within a season and how this depends on relations in prior seasons with sm providing the cross-seasons memory. In this paper, we will exploit the distinction between future best and worst cases to identify how summer sm is influenced by precipitation year-round. We will also use the grand ensemble mean across all PDO and AMO combinations to isolate the radiatively forced changes. Since the hydrological adjustment (defined as the adjustment to a new balance in the land–atmosphere system between sm tendency, P, and ET and between $P - \mathrm{ET}$ and moisture convergence in the atmosphere) depends on summer precipitation, which has regions of both increase and decrease in the domain, we will also examine the causes of this by performing a moisture budget decomposition. Last, since a radiatively forced decline in fall precipitation is important to precondition winter sm, we will examine its mechanisms in terms of the moisture budget.

2. Model simulations and moisture budget analysis

a. The SST-forced large boundary value ensemble

The model simulations used here were described at length in Seager et al. (2023) and will only be briefly summarized here. The model used is a lower resolution (1.9° × 2.5°, 32 levels), no-aerosol chemistry, version of the National Center for Atmospheric Research Community Atmosphere Model, version 6 (CAM6), coupled to the Community Land Model, version 5 (Danabasoglu et al. 2020). As such, the atmosphere and land surface are fully coupled via water and energy fluxes, but the atmosphere–land system is forced by the imposed ocean conditions. A historical 16-member ensemble was run from January 1979 through August 2021 with different initial conditions for each ensemble member. Projections for the future begin in January 2021 and run through December 2041.

A collection of boundary value ensembles is produced forced by different scenarios for SST. The 800 scenarios for 21-yr period SST evolution due to the PDO, AMO, and El Niño–Southern Oscillation (ENSO) were generated using a linear inverse model (LIM) trained on the historical SST data. The scenario generation accounts for the coupling between the PDO and ENSO but treats the AMO as being independent. From these, three groups of 16 were selected that have the strongest positive PDO, strongest negative PDO, and most neutral states of the PDO, quantified as the 20-yr average of their PDO indices. We also required that the 16 PDOs have similar time evolution over the period and no strong trend. These 16 scenarios have similar PDOs but different, realistic, ENSO cycles. For the AMO, we select the single SST scenarios with the most positive, most neutral, and most negative states for the 2021–41 period and no strong trend over the 20-yr period. The PDO-plus-ENSO and AMO states are combined to generate 16 global SST scenarios for each combination of the PDO and AMO.

These presumed natural variations of SST are added to estimates of the radiatively forced change. For one "grand ensemble," defined as the collection of 16-member ensembles with different PDO and AMO combinations (also referred to as "all"), the forced SST imposed is taken from phase 6 of the Coupled Model Intercomparison Project (CMIP6) multimodel ensemble mean. For the other grand ensemble, the observed Hadley Centre SST history is extrapolated forward based on regression to total greenhouse gas (GHG) forcing. The CMIP6 estimate has enhanced warming in the equatorial Pacific cold tongue, while the Hadley-based estimate continues forward the observed pattern of no warming of the cold tongue.

For each PDO and AMO combination, and each grand ensemble, we have 16 SST scenarios that have slightly different PDO and independent ENSO evolutions but the same AMO and forced SST evolution. The climate model is forced with these 16 scenarios to generate the collection of 16-member boundary-forced ensembles analyzed here. The ensemble members are additionally forced by the changes in land use/land cover and radiative forcing consistent with the CMIP6 shared socioeconomic pathways (SSP) 370 scenario. The mean across the PDO and AMO combination ensembles will identify the common, atmosphere–land changes driven by the imposed estimates of radiatively forced SSTs, land use/land cover, and radiative forcing. This will be referred to as the radiatively forced change whether for the Hadley-based or CMIP6-based forced SST estimates.

Here, we will primarily focus on the result using the Hadley-based forced SST trend estimate, which favors a decline in cool season precipitation over SWNA. For that result and details of these computations and model setups, the reader is referred to Seager et al. (2023). In this paper, we will examine best-case, worst-case, and grand ensemble mean scenarios. Based on the analysis shown in Seager et al. (2023), the best-case scenario is defined as a positive PDO (warm tropical Pacific) and a negative AMO (cool subtropical North Atlantic), denoted as PDO+AMO−, while the worst case is defined as the opposite phases of the PDO and the AMO and denoted as PDO−AMO+. The grand ensemble all case averages over the following scenarios: PDO+AMO+, PDO−AMO+, PDO+AMO−, PDO−AMO−, and PDO0AMO0, using the same denotation and additionally 0 to denote neutral. All contains 16 × 5 = 80 ensemble members.

All data shown are for differences within a season [December–February (DJF), March–May (MAM), June–August (JJA), and September–November (SON)] for the next decade, 2031–41, minus the historical period, 1979–2021. For the geopotential height differences, the area-weighted global mean is subtracted to remove an overall signal of heights rising with atmospheric warming and expansion. The sm is evaluated as the total water in the upper 1 m of the model soil layers.

For an area average, we use the land points within a box that covers 25°–40°N, 125°–100°W. The box is shown in all maps as a rectangle but no data from ocean points within it are used.

b. *Analysis of the model moisture budget*

We will analyze the changes in the transports and convergences/divergences of moisture in the atmosphere that couple to the changes in the land surface hydrology via P and ET at the surface. The change, denoted by Δ and being the 2031–41 period minus the 1979–2021 period, in the vertically discretized moisture budget is

$$\Delta(\overline{\overline{P}} - \overline{\overline{\mathrm{ET}}}) \approx -\Delta\left[\frac{1}{g\rho_w}\nabla\cdot\sum_{k=1}^{K}\overline{\overline{(\overline{\mathbf{u}}_k\overline{q}_k + \overline{\mathbf{u}'_k q'_k})\overline{dp}}_k}\right]. \tag{1}$$

Here, the ET equals evaporation over the ocean, g is the gravity, ρ_w is the water density, p is the pressure, p_s is its surface value, q is the specific humidity, $\mathbf{u}$ is the vector velocity along pressure surfaces, k refers to the vertical level of which there are K total, and dp_k is the pressure thickness of each level with the lowest level extending to p_s. Monthly means are represented by overbars, departures from monthly means are represented by primes, and climatological monthly means are represented by double overbars. The first term on the right-hand side is the moisture convergence by the mean flow and the second term is that by the transient eddies. Covariances of flow and humidity are saved at the time step level and saved as monthly means. The notation follows that of Seager and Henderson (2013) and Seager et al. (2012, 2014a,b).

If we denote the historical values of quantities with a 20 subscript, e.g., $q_{20,k}$ (referring to the twentieth century), then we can divide up the mean flow moisture convergence change into that due to changes in flow ("dynamic") and that due to changes in humidity ("thermodynamic"), neglecting the nonlinear term, viz.,

$$\begin{aligned}-\Delta\left(\frac{1}{g\rho_w}\nabla\cdot\sum_{k=1}^{K}\overline{\overline{\mathbf{u}}_k\overline{q}_k\overline{dp}}_k\right) \approx{}& -\Delta\left(\frac{1}{g\rho_w}\nabla\cdot\sum_{k=1}^{K}\overline{\overline{\mathbf{u}}_k\overline{q}_{20,k}\overline{dp}}_k\right)\\ &- \Delta\left(\frac{1}{g\rho_w}\nabla\cdot\sum_{k=1}^{K}\overline{\overline{\mathbf{u}}_{20,k}\overline{q}_k\overline{dp}}_k\right).\end{aligned} \tag{2}$$

The dynamic and thermodynamic terms can further be divided into terms associated with divergent flow, advection across moisture gradients, and a surface term, viz.:

$$\begin{aligned}-\Delta\left(\frac{1}{g\rho_w}\nabla\cdot\sum_{k=1}^{K}\overline{\overline{\mathbf{u}}_k\overline{q}_{20,k}\overline{dp}}_k\right) = -\frac{1}{g\rho_w}\Bigg[&\sum_{k=1}^{K}\overline{\Delta(\nabla\cdot\overline{\mathbf{u}}_k)\overline{q}_{20,k}\overline{dp}}_k\\ &+ \sum_{k=1}^{K}\overline{\Delta\overline{\mathbf{u}}_k\cdot\nabla\overline{q}_{20,k}} + S_{\mathrm{DYN}}\Bigg],\end{aligned} \tag{3}$$

$$\begin{aligned}-\Delta\left(\frac{1}{g\rho_w}\nabla\cdot\sum_{k=1}^{K}\overline{\overline{\mathbf{u}}_{20,k}\overline{q}_k\overline{dp}}_k\right) = -\frac{1}{g\rho_w}\Bigg[&\sum_{k=1}^{K}\overline{\nabla\cdot\overline{\mathbf{u}}_{20,k}\Delta\overline{q}_k\overline{dp}}_k\\ &+ \sum_{k=1}^{K}\overline{\overline{\mathbf{u}}_{20,k}\cdot\nabla\Delta\overline{q}_k} + S_{\mathrm{TH}}\Bigg].\end{aligned} \tag{4}$$

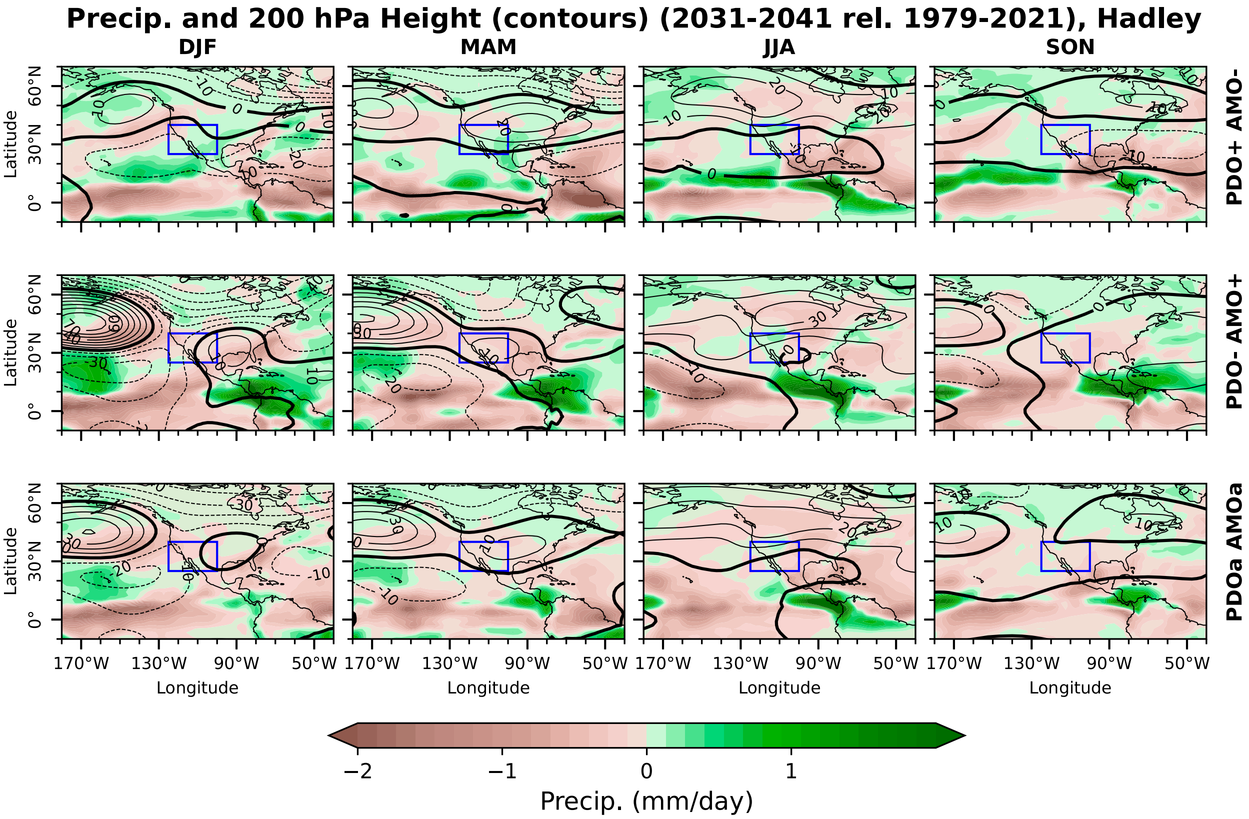

FIG. 1. The P (colors; mm day^{-1}) and 200-hPa heights (contours; m) for the (top) best case (PDO+AMO−), (middle) worst case (PDO−AMO+), and (bottom) for the grand ensemble averaged across all the PDO and AMO combination ensembles, for 2031–41 relative to 1979–2021, and each season, using the Hadley-based forced SST projections.

The S_{DYN} and S_{TH} terms are surface terms of the form $\bar{\mathbf{u}}q_s\cdot\nabla p_s$, and the equalities in Eqs. (3) and (4) are justified since they can be evaluated reasonably as a residual of the other two terms in each equation [see Seager and Henderson (2013) for a demonstration of this]. This analysis method will be used below to diagnose the causes of changes in $P - \mathrm{ET}$ over SWNA (and the wider North American region) in summer and fall and their relation to changes in circulation and humidity and to divergent and advective mechanisms.

3. Large-scale ocean–atmosphere–land surface changes over the Pacific and North America for the next decade

Figure 1 shows maps of changes in precipitation and 200-hPa heights for each season and 2031–41 relative to 1979–2021 and for best-case, worst-case, and all scenarios. Given that this is for the Hadley-based future SST scenario, all cases show a region of reduced precipitation in the equatorial Pacific consistent with the lack of warming of the cold tongue amid more general warming. Tropical Pacific drying is more extensive in the negative PDO case than in the positive PDO case due to its cooler underlying SSTs. The worst-case scenario (Fig. 1, middle row) shows a classic Pacific–North America (PNA)–like teleconnection in the cool season with low heights in the subtropical North Pacific, a high over the extratropical North Pacific, a low over Canada, and another high over the southeast United States. This height pattern would displace the Pacific jet stream poleward and also place northerly subsiding flow on the west coast. The whole of the western United States and Mexico have reduced winter and spring precipitation in this case. In the best case (Fig. 1, top row), with a positive PDO and negative AMO, the PNA-like teleconnection is not apparent and parts of the southwest have increased cool season precipitation. However, there is still a weak high over the North Pacific, despite the low that we would expect the positive PDO to induce. This is because of the additional presence of radiative forcing. In the all case (Fig. 1, bottom row) which averages across all the states of the PDO and AMO, there is also a PNA-like teleconnection with a strong North Pacific high. This originates from the lack of cold tongue warming in the Hadley-based future scenario which, amid more general warming, is a loosely La Niña–like pattern.

Figure 2 shows the future minus past differences in SST, sm (over land), and 700-hPa heights. The imprints of the PDO and AMO are clearly apparent in the SSTs with the cooler tropical Pacific for negative PDO cases and the cooler North Atlantic for negative AMO cases. The lack of equatorial Pacific warming is also evident in the best and worst cases and in the all cases and derives from extrapolating forward the observed

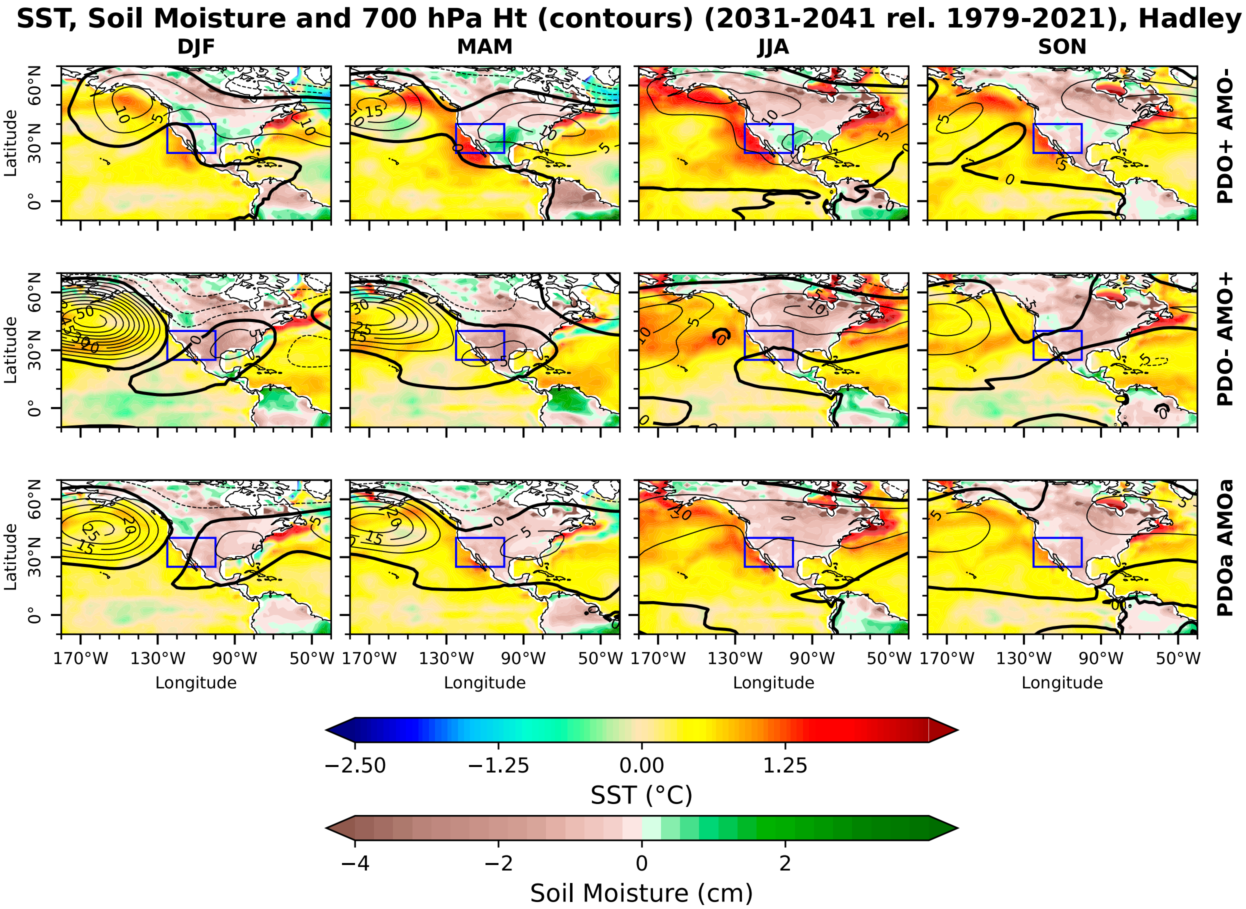

FIG. 2. SST (colors over ocean; K), 700-hPa heights (contours; m), and sm (colors over land; cm) for the (top) best case (PDO+AMO−), (middle) worst case (PDO−AMO+), and (bottom) averaged across the entire ensemble, for 2031–41 relative to 1979–2021, and for each season, using the Hadley-based forced SST projections.

SST trend pattern. During the cool season, the height anomalies at 200 hPa are reflected at 700 hPa. In summer and fall, the PNA-like pattern is not evident, and instead, we see a weaker zonally elongated ridge centered over Canada (fall in the worst case is an exception).

In summer, all the cases show a pattern of increased precipitation in the northwest portion of SWNA and decreased precipitation in the southeast portion of the region (Fig. 1, third column). This must be a radiatively forced response given its presence in all PDO and AMO cases. In fall, reduced precipitation occurs across most of SWNA in all cases and again must be a radiatively forced response (Fig. 1, right column). The sm is influenced by precipitation change, and the best case has increases in some parts of the southwest in winter and spring and a mixed signal in summer and is mostly reduced in fall (Fig. 2, top row). In contrast, the worst case and the all case have reduced sm year-round.

4. Cross-seasons development of changes in the land–atmosphere hydrological state

The above results demonstrated the sm and *P* change across seasons and illustrated the large-scale ocean–atmosphere changes that drive the cool season precipitation changes. To understand how changes in *P*, ET, sm, air humidity, and VPD propagate across seasons, in Fig. 3, we present scatterplots of different variables either concurrently or with some leading others. Each data point represents the difference between the future period (2031–41) and the historical climatology (1979–2021) for each member of the grand ensemble.

We start by showing changes in cool season *P* (*y* axis) versus summer sm (*x* axis) with data points colored to show the change in, intervening, spring ET (Fig. 3a). On this and all panels in Fig. 3, the shape of the data points shows the PDO and AMO combination of that ensemble member. What is immediately apparent is that summer sm changes are well predicted by cool season *P* changes: Less winter and spring *P* lead to drier soils in summer. The worst-case scenarios (downward triangles) have reduced cool season *P*, while the best-case scenarios (upward triangles) tend to have increased cool season *P*. The worst-case *P* decline clearly propagates into drier summer soils, while the best-case scenarios have summer sm changes scattered around zero even though cool season *P* increased. This is due to the influence of changes in ET. Spring ET declines in the case of strong drops in cool season *P* as a response to declining moisture availability. However,

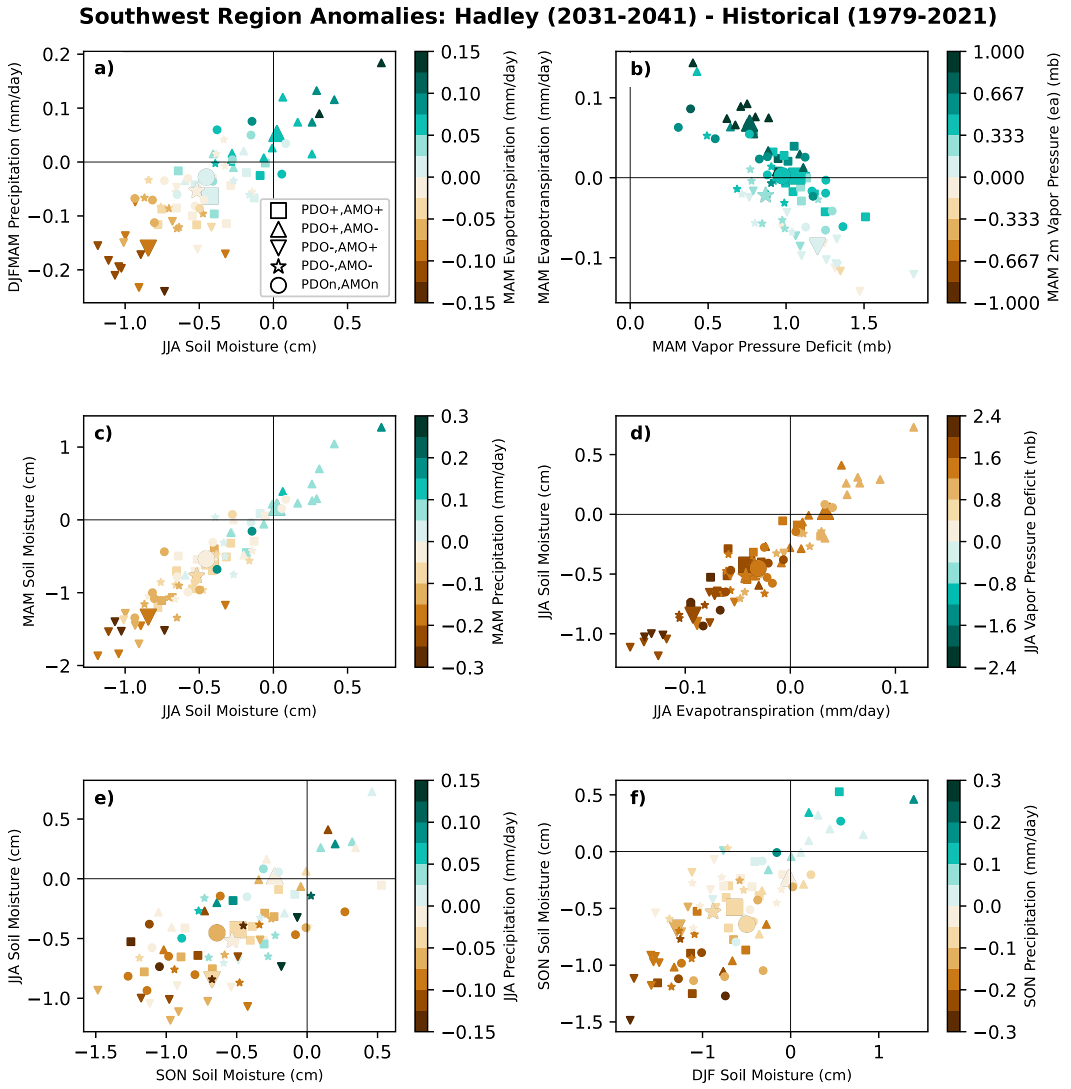

FIG. 3. Scatterplots of changes in (a) cool season P vs following summer sm with spring ET colored, (b) spring ET vs spring VPD with spring e_a colored, (c) spring sm vs following summer sm with spring P colored, (d) summer sm vs summer ET with summer VPD colored, (e) summer sm vs following fall sm with summer P colored, and (f) fall sm vs following winter sm with fall P colored. Units are millimeters per day for P and ET and centimeters for sm.

we also see that spring ET increases for more moderate declines in cool season P and always increases if the cool season P increases.

In spring (Fig. 3b), surface air humidity essentially always increases even in cases with reduced cool season P, reflecting atmospheric warming and rising moisture holding capacity. Spring ET tends to decrease for the worst-case and increase for the best-case scenarios, clearly following cool season P changes: Heightened moisture availability leads to more spring ET. In spring, the higher the ET, the higher the air humidity and the lower the VPD. These cool season and spring relations can be explained as follows. In cases where cool season P strongly reduces, spring ET reduces, air humidity increases are restricted, and VPD increases are large. By contrast, in cases where cool season P increases, it drives an increase in spring ET and air humidity increases sufficiently to limit VPD increases.

Figure 3c shows that spring sm, which in most cases is drying, predicts summer sm well. This preponderance of drying in spring and summer is accompanied by a decline in spring P. Summer sm decline is associated with a decline in ET (Fig. 3d), and the drier the soils and the more reduced the ET, then the higher the VPD is. In summer, although the large majority of cases have drying soils, sm drying is more extreme when summer P also reduces (Fig. 3e). Summer sm increases are limited primarily to some of the best-case ensemble members with increased cool season P (Fig. 3a). In those small number of cases with increased summer sm, summer ET increases and VPD increases are small.

Summer sm well predicts fall sm but with the driest soils in fall going along with the cases with reduced summer P (Fig. 3e).

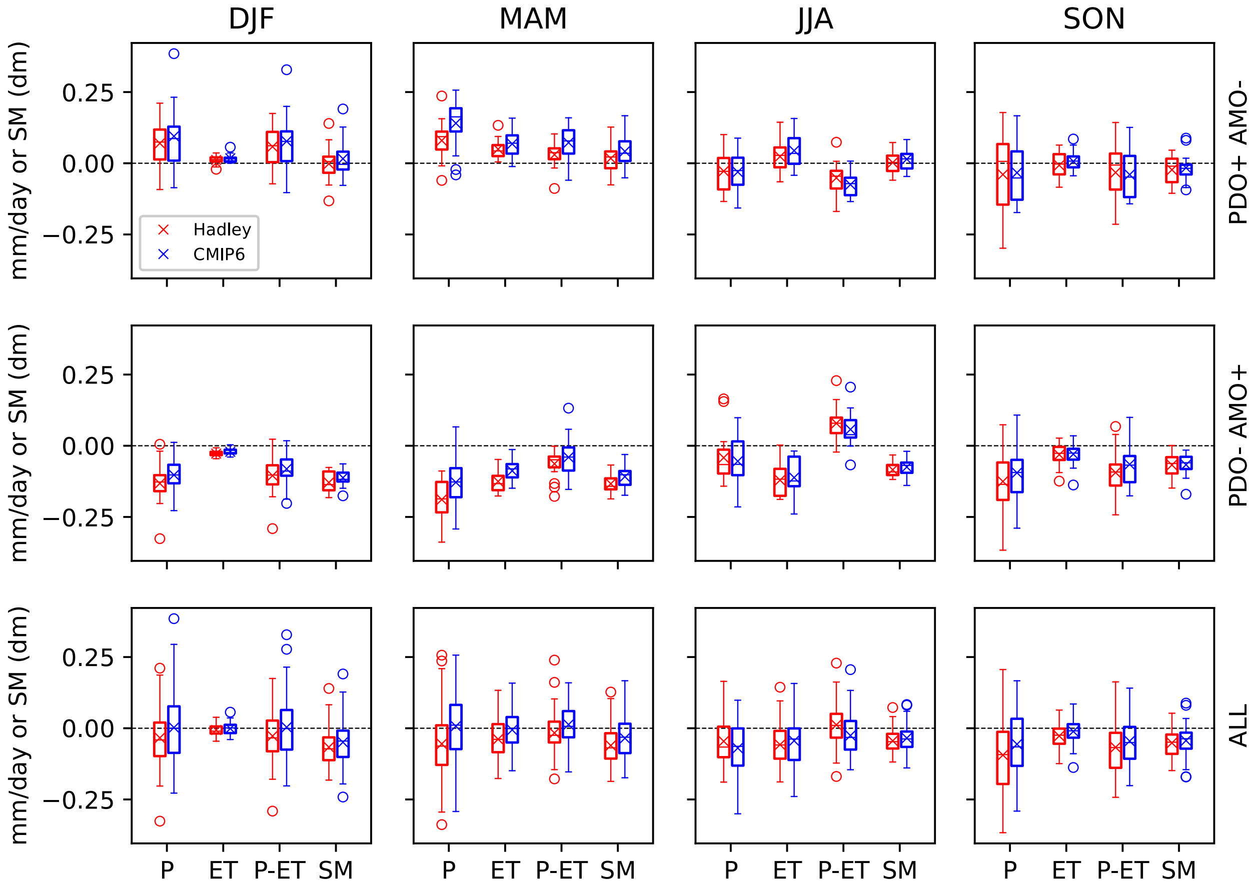

FIG. 4. Box-and-whisker plots of changes in P, ET, and $P-\mathrm{ET}$ and sm for the (top) best-case, (middle) worst-case, and (bottom) all scenarios for (from left to right) winter, spring, summer, and fall. Results from both the Hadley- and CMIP6-based forced SST projections are shown. The limits of the boxes are the 25th and 75th percentiles of the range across ensemble members, the horizontal line is the median, the cross is the mean, the whiskers denote the range, and circles indicate the outliers. Units are millimeters per day for P, ET, and $P-\mathrm{ET}$ and decimeters for sm.

In the fall, almost all ensemble members across PDO and AMO states have reduced P which, therefore, must be radiatively driven, and the greater the P drop, the more the decline in fall sm. Completing the propagation of influence across seasons, fall P reduction is a good predictor of winter sm reduction. Winter sm loss, even in many of the best-case scenario members with increased winter P (Fig. 4, below), comes about from this robust decrease in fall P (Fig. 3f).

Figure 4 presents an alternate way to see the cross-season progression of changes in the land–atmosphere system in the form of box-and-whiskers plots showing changes in mean, median, and spread of the ensembles. For the best-case scenario (Fig. 4, top row), an increase in winter P overwhelms an increase in ET and positive $P-\mathrm{ET}$ is associated with a small increase in sm. In spring, ET rises but P rises by even more and positive $P-\mathrm{ET}$ further increases sm. The sm declines in summer as reduced P and increased ET, allowed for by wet soils, combine to create strongly negative $P-\mathrm{ET}$. Fall decrease in P further reduces sm. Dry soils inherited from fall are why the winter increase in P does not lead to appreciably wetter soils in winter. (The ratio of runoff to P actually tends to decrease modestly, which would increase sm, and hence changes in runoff are not causes of drying sm.)

The worst-case scenario is starkly different. In this case, winter decline in P and $P-\mathrm{ET}$ drives drier soils. In spring, P declines, but now ET also declines, responding in a regulating manner to the drier soils, such that the $P-\mathrm{ET}$ decline is more modest but dry soils persist. In summer, the decline in ET responding to dry soils is so large that it overwhelms the decrease in P and positive $P-\mathrm{ET}$ actually increases sm above the spring values but remaining dry. Radiatively forced fall decline in P then forces reduced $P-\mathrm{ET}$ and further soil drying that persists into winter.

In the all case that isolates the common radiatively forced response, the decline in P in summer and fall drives the hydrological response with reduced ET partially offsetting but allowing reduced sm year-round.

Figure 4 shows results for both the case with Hadley-based forced SST projections, which we have focused on above, and for the case with CMIP6-based projections. The P changes are generally more negative for the Hadley case, because of its continued lack of warming of the equatorial Pacific cold

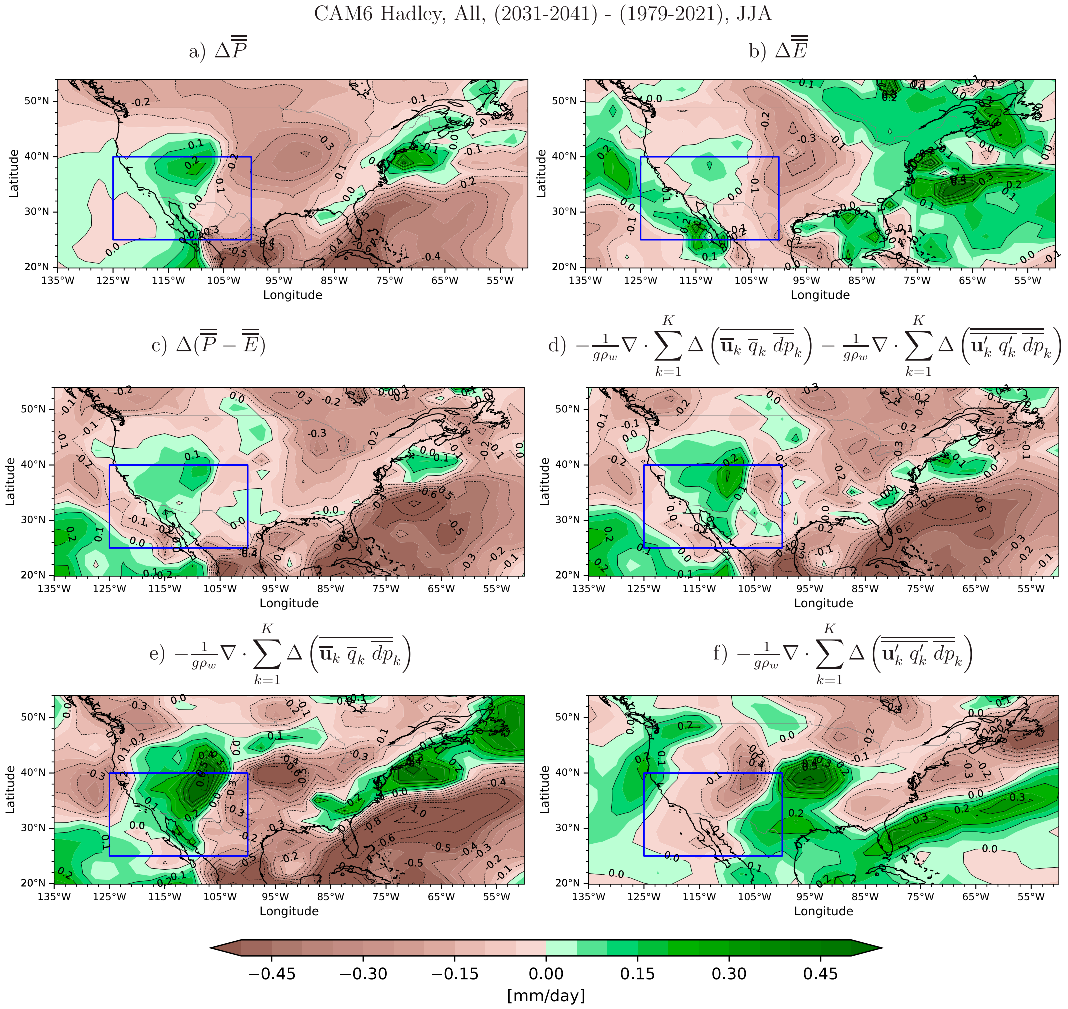

FIG. 5. Moisture budget breakdown for changes in summer for all scenarios. Changes in (a) P, (b) ET, (c) $P-$ ET, (d) the sum of moisture convergences by mean and transient flow, (e) the contributions of the mean, and (f) transient flow moisture convergence. All units are millimeters per day.

tongue, than for the CMIP6 case which has cold tongue warming. This P difference propagates into drier soils year-round in the Hadley-based projections across the scenarios.

5. Mechanisms for summer precipitation change

As just shown, for the SWNA area average, in best, worst, and all scenarios, there is a decline in summer P. Since it is common across the grand ensemble, it is radiatively forced. Figures 1 and 5 make clear this decline is actually made up of a wetting/drying change in P in the northwest/southeast of the SWNA box. Here, given that summer hydroclimate changes have received less attention than cool season ones, we seek to explain this phenomenon and use the Hadley-based all scenario since all best represents the radiatively forced changes common to all the different PDO and AMO scenarios. Figure 5 shows the moisture budget component changes for North America. While P reduces across most of the continent, it increases in the southwest in California, Nevada, Utah, and Arizona and the western reaches of New Mexico and Colorado. This area is also one of positive $P-$ ET (Fig. 5c) indicating that it must have a positive moisture flux convergence change. In contrast, the region of decline of P to the immediate east is largely sustained by a decline in ET (Fig. 5b) with little change in $P-$ ET and, hence, moisture flux convergence (Fig. 5c).

In Fig. 5, we shed light on the mechanisms involved by breaking down the moisture budget. Convergence of moisture by the mean plus transient flow (Fig. 5d) balances $P-$ ET (Fig. 5c). The wetting in $P-$ ET over the west of SWNA is maintained by mean flow moisture convergence (Fig. 5e) and opposed by transient eddy moisture divergence (Fig. 5f). The weaker change in $P-$ ET in the east of SWNA actually arises from a strong cancellation between mean flow moisture divergence and transient eddy moisture convergence. In general, across the Pacific–North America–Atlantic domain, the transient eddy moisture convergence/divergence is opposing—and hence responding to—what the mean flow is inducing. In the SWNA region, the local maximum in humidity increase stretching from

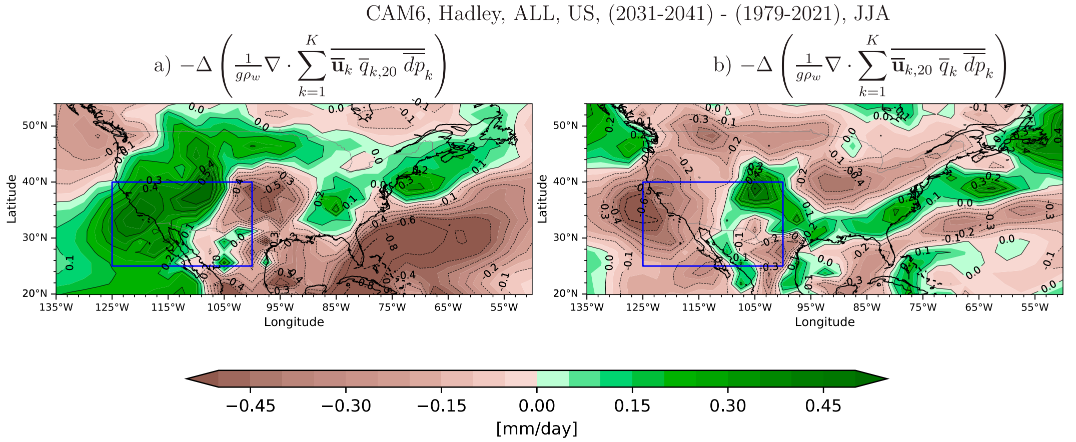

FIG. 6. The mean flow moisture convergence change divided into components due to changes in (left) circulation (dynamic) and (right) humidity (thermodynamic). All units are millimeters per day.

the southwest to the north-central part of the region (Fig. 8c) is opposed by transient eddy moisture divergence (Fig. 5f), while the local minimum in humidity increase in the east of the region is opposed by transient eddy moisture convergence.

The change in mean flow moisture convergence could arise from a change in humidity (thermodynamic) or a change in the mean flow (dynamic), and these two terms are shown in Fig. 6. It is the dynamic term (Fig. 6a) that drives the west-wetter and east-drier change over SWNA and is in general responsible for the mean flow moisture convergence changes across the domain. The mean flow moisture convergence changes could arise themselves from either changes to the component involving mass convergence or the component involving moisture advection. The dynamic and thermodynamic contributions to convergence and advection terms are shown in Fig. 7. Changes in humidity contribute little to the divergent term (Fig. 7b) but provide a drying across most of SWNA via the advection term (Fig. 7d). However, the wet-west and dry-east feature is generated by the change in the mean flow advecting the unchanged moisture field wetting the west (Fig. 7c), while a changed divergent flow dries the east (Fig. 7a).

To show how these changes to the moisture budget occur, in Fig. 8, we show the changes in winds at 700 and 850 hPa mapped over the climatological vertically integrated humidity field and the climatological winds mapped over the change in vertically integrated humidity. The thermodynamic advective drying across most of the domain (Figs. 7a,d) arises from mean low-level winds—northerlies at 850 hPa in the northwest and southerlies at 850 hPa in the southeast—flowing from regions of lesser to greater humidity increase (Fig. 8c).

Turning to the dynamics changes, while the mean winds over the United States are westerly (Fig. 8a), the change in winds is easterly (Fig. 8b). This relates to the zonally oriented high pressure anomaly that develops across the North Pacific and northern North America (Fig. 1; JJA; bottom row) with easterly winds on its southern flank [this is also seen in the multimodel analysis of summer circulation response to idealized warming experiments of Li et al. (2018), supplemental information]. Since the climatological humidity gradient is drying toward the west, these wind anomalies induce wetting in the west of SWNA where the gradient is strong. The same term induces weaker drying to the east which is due to south-southwesterly lower-level flow from climatologically drier to wetter regions (Fig. 8d). However, due to topography, this is not entirely clear and a full explanation would need exploration of the covariation with height of the mean humidity and changed flow field. Nonetheless, enhanced low-level divergence generates much of the drying in the east of SWNA (Fig. 7a). The divergence can be deduced from the changes in the winds at 700 and 850 hPa (Figs. 8b,d), where southerly anomalies at 850 hPa and southeasterlies at 700 hPa generate divergence across the eastern part of SWNA. The subsidence here is part of a broader region of mean flow moisture divergence that extends over the Gulf of Mexico, Florida, and the western subtropical Atlantic Ocean. All of this is related to northeasterlies equatorward of the extratropical ridge anomaly.

Figure 8 also shows the changed vertically integrated humidity field which contains considerable spatial structure. There is a notable minimum in the increase of humidity extending west from the subtropical west Atlantic across Florida, then south of the Gulf Coast into Texas and northward across the eastern part of SWNA (Figs. 8a,c, shading). This feature matches the region of anomalous mean flow moisture divergence due to anomalous divergence (Fig. 7a). However, over land, it is largely cancelled out by enhanced transient eddy moisture convergence (Fig. 5f) and does not translate into a large change in $P-\mathrm{ET}$ (Fig. 5c). The eddy moisture fluxes oppose what the mean flow is generating.

To summarize, the region-mean summer change SWNA is a reduction in P, but this is comprised of an increasing region in the northwest and a decreasing region in the eastern portions of the region. The wetting region in the northwest is reflected in a positive change in $P-\mathrm{ET}$ and hence requires a moisture convergence anomaly. The drying region in the east goes along with reduced ET and little change in $P-\mathrm{ET}$ and, hence, little change in moisture convergence. The wetting in

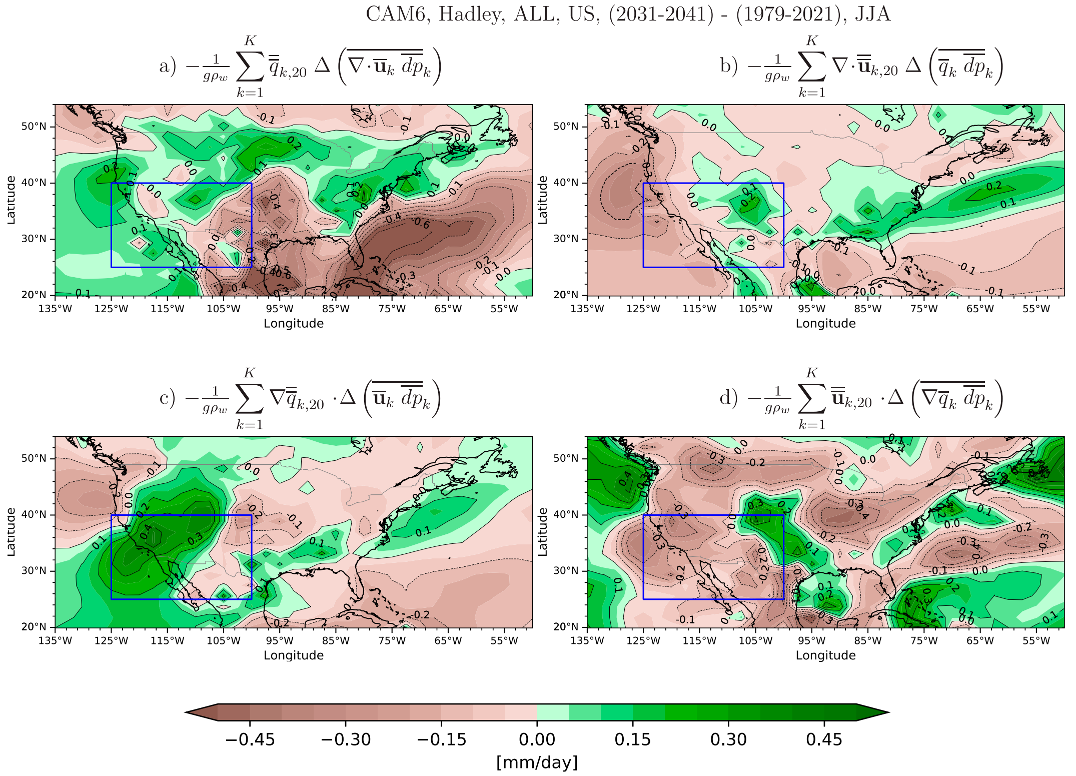

FIG. 7. The (a),(c) dynamic and (b),(d) thermodynamic divided into contributions from the (a),(b) convergent flow and (c),(d) change in advection across moisture gradients. All units are millimeters per day.

the northwest is ultimately dynamically induced by the anomalous extratropical ridge, while the drying in the east is induced by a reduction in ET with a low-level mean flow divergence anomaly opposed by transient eddy moisture divergence.

6. Mechanisms for fall precipitation change

Figure 9 shows the moisture budget breakdown for SON. In this case, there is a widespread decrease in P across the western and southern United States (Fig. 9a) which, due to more modest changes in ET (Fig. 9b), translates into widespread reductions in $P - \mathrm{ET}$ (Fig. 9c). While anomalous mean flow moisture divergence contributes to drying in the west of SWNA (Fig. 9e), anomalous transient eddy moisture divergence dries across the United States (Fig. 9f). Unlike for summer, in fall, the changes in mean flow and transient eddy moisture convergence are not offsetting over SWNA.

Changes in transient eddy moisture divergence can arise from either changes in the strength and location of eddies and/or change in the gradients in the humidity fields that they are operating in. To separate these effects, we adopt a mixing length theory approach as in Ting et al. (2021). We assume that the humidity perturbations in a transient eddy due to zonal and meridional displacements can be approximated by $q' \approx L_x\partial\overline{q}/\partial x$ and $q' \approx L_y\partial\overline{q}/\partial y$. The length scales L_x and L_y are approximated by $u'\tau$ and $v'\tau$, with τ a time scale, such that the eddy moisture fluxes can be written as

$$\overline{u'q'} \approx -\tau\overline{u'^2}\partial\overline{q}/\partial x, \tag{5}$$

$$\overline{v'q'} \approx -\tau\overline{v'^2}\partial\overline{q}/\partial y. \tag{6}$$

The transient eddy moisture flux convergence is then approximated as

$$-\frac{1}{g\rho_w}\nabla\cdot\int_0^{p_s}\overline{\mathbf{u}'q'}\,dp = \frac{\tau}{g\rho_w}\left(\frac{\partial}{\partial x}\int_0^{p_s}\overline{u'^2}\frac{\partial\overline{q}}{\partial x}dp + \frac{\partial}{\partial y}\int_0^{p_s}\overline{v'^2}\frac{\partial\overline{q}}{\partial y}dp\right). \tag{7}$$

Note that this estimation considers the covariation with height of the eddy field and the mean moisture gradients. Representing quantities as before as the sum of the past values and the future change, the transient eddy moisture convergence change can be written as the sum of components due to changes in eddy activity ("ΔEDDIES") and changes in humidity gradient ("ΔQGRAD"), viz:

$$-\Delta\left(\frac{1}{g\rho_w}\nabla\cdot\int_0^{p_s}\overline{\mathbf{u}'q'}\,dp\right) \approx \Delta\mathrm{EDDIES} + \Delta\mathrm{QGRAD}, \tag{8}$$

$$\Delta\mathrm{EDDIES} = \frac{\tau}{g\rho_w}\left(\frac{\partial}{\partial x}\int_0^{p_s}\Delta\overline{u'^2}\frac{\partial\overline{q}_{20}}{\partial x}dp + \frac{\partial}{\partial y}\int_0^{p_s}\Delta\overline{v'^2}\frac{\partial\overline{q}_{20}}{\partial y}dp\right), \tag{9}$$

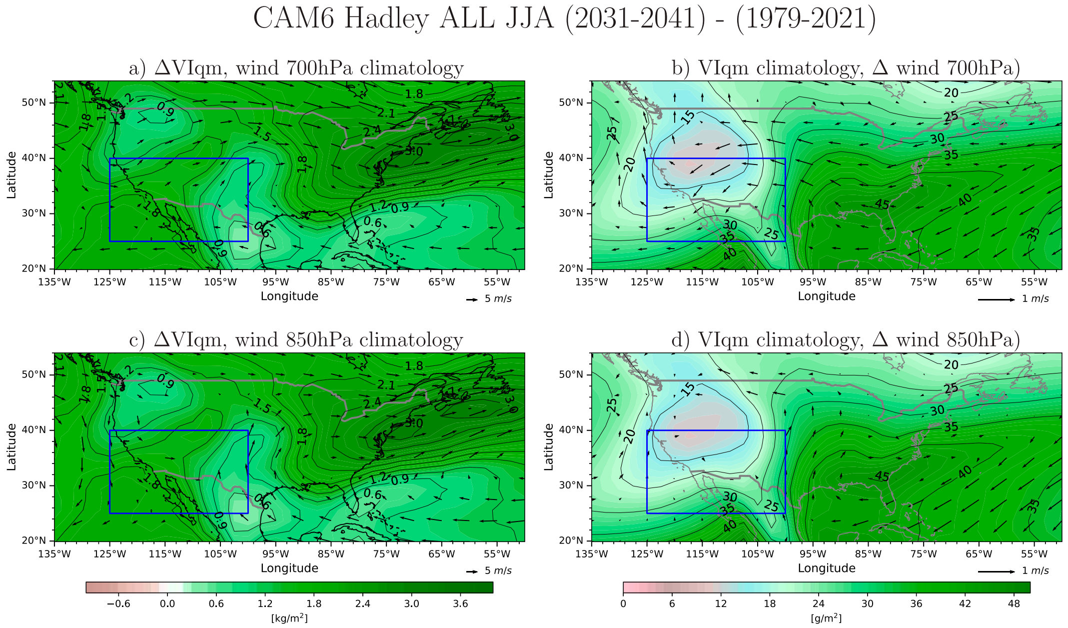

FIG. 8. The change in vertically integrated moisture content with the (a) 700- and (c) 850-hPa wind climatology and the climatological vertically integrated moisture and the change in (b) 700- and (d) 850-hPa winds. Moisture in grams per meter squared and wind speeds in meters per second with reference vector at the bottom right.

$$\Delta\mathrm{QGRAD} = \frac{\tau}{g\rho_w}\left(\frac{\partial}{\partial x}\int_0^{p_s}\overline{u_{20}'^2}\frac{\partial\Delta\overline{q}}{\partial x}dp + \frac{\partial}{\partial y}\int_0^{p_s}\overline{v_{20}'^2}\frac{\partial\Delta\overline{q}}{\partial y}dp\right). \tag{10}$$

In the above, we ignore the nonlinear term involving changes in both humidity and eddies.

We evaluate the SON climatological seasonal mean left-hand side and right-hand side (without τ) of Eq. (7) for model grid points in the domain of North America and the immediately adjacent seas (135°–50°W, 30°–50°N). We then plot these against each other together with the least squares best fit line, the slope of which provides an estimate of τ. This relation is shown in Fig. 10a. With the estimate for τ, we then compute the change in transient eddy moisture convergence in SON using Eq. (7) and show this in Fig. 10b to be compared to the actual change in Fig. 9f. It is hardly surprising that the comparison reveals many differences given the simple assumptions made in the mixing length estimation. However, we believe it justifies performing the breakdown into changes in eddies and changes in the mean humidity gradients, shown in Figs. 10c and 10d. As seen in Fig. 10e (contours), the eddies weaken everywhere, and hence, whatever they were doing in the climatology, they will be doing less of in the future. For example, since they diffuse the mean humidity gradient (Fig. 10e, colors) by drying the western Atlantic and moistening the eastern continent, the change due to change in eddies dries the continental margin and moistens the west Atlantic (Fig. 10c). For the past climatology, transient eddies wet the coast of SWNA, and the change induced by weaker eddies, therefore, leads to drying in this region. Some of the transient eddy drying over SWNA, however, results from the change in mean humidity gradients. In this case, since there is an eddy field across North America, strengthening from south to north and with maxima in the northwest and northeast (Fig. 10f, contours), we expect the change to be a diffusion of the changed humidity field (Fig. 10f, colors). This is clear in the tongue of minimum increased humidity over the Gulf of Mexico and Florida, where the humidity gradient–induced change moistens, and the area of maximum increased humidity over the Plains and southeast United States, where the humidity gradient–induced change dries (Fig. 10d). Transient eddy drying over the central and western northern United States, which extends into the northern part of SWNA, is also acting to diffuse a local maximum humidity increase.

The mixing length approximation is clearly just that, an approximation. But what this qualified analysis makes clear is that the drying SWNA by transient eddy moisture divergence (and more broadly of most of the United States) in SON arises from a combination of weakening storm systems and altered moisture gradients. Since the changed moisture gradients are themselves a response to thermodynamic processes (moistening with warming) and dynamic processes (e.g., moistening in regions of anomalous mass convergence and/or anomalous advection from wetter areas), the underlying mechanisms involve coupling between the atmospheric circulation and the hydrological cycle. (For example, the change in 700-hPa winds shown as vectors in Fig. 10f shows anomalous mass divergence in the Gulf of Mexico tongue of low humidity increase. As a second example, onshore easterly flow anomalies increase humidity over the eastern United States.) However, returning to the connections across seasons, this storm system–driven drying in the fall sets up for the following season the decline of winter sm in the worst-case and all scenarios and

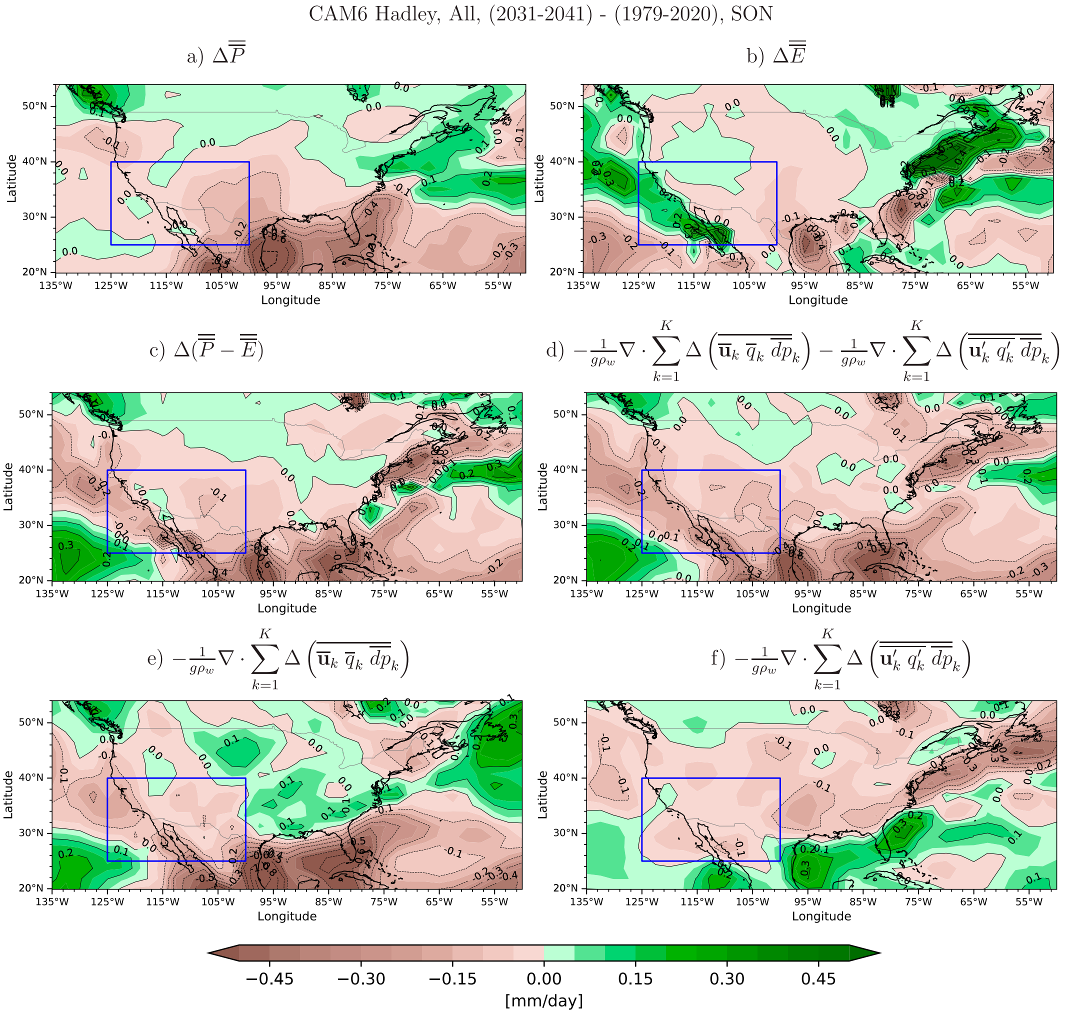

FIG. 9. As in Fig. 5, but for SON. All units are millimeters per day.

the minor increase of sm in the best case despite increased winter precipitation.

7. Conclusions

We have investigated the connections across seasons in the ocean–atmosphere–land system that lead to likely aridification, defined as summer sm decline, in SWNA in all but the best-case scenarios for the next two decades. This work was performed using a novel set of modeling experiments. An atmosphere model was forced by a set of scenarios for future SSTs that combined estimates of the radiatively forced response with realistic variations due to the PDO, AMO, and ENSO. This boundary value ensemble allows us to assess a full range of plausible future climate trajectories, including best-case, worst-case, and middle-of-the-road scenarios for drought in SWNA. As previously reported (Seager et al. 2023), even in a best-case scenario of a shift to the warm phase of the PDO and cool phase of the AMO, the hydroclimate of SWNA never returns to the levels of summer sm typical of the late twentieth century, while in the worst case (cool tropical Pacific, warm North Atlantic), soils in summer continue to dry. Building on that work, here, we have examined how that heightened aridity is generated by changes in precipitation, evapotranspiration, and sm across seasons. Since changes in summer and fall are critical, we also determine how changes in precipitation and evapotranspiration in those seasons are enabled by changes in the mean and transient atmospheric circulation and moisture transports as a response to radiative forcing. The main conclusions are as follows.

- Precipitation over SWNA in the next decade will be highly dependent on the future of decadal ocean variability. While the effects of radiatively forced climate change, identified as the mean across all the ensembles, for both observations and CMIP6-based forced SST projections, are to reduce precipitation in the region year-round, in the best-case scenario, cool season precipitation increases while it strongly declines in the worst-case (cool tropical Pacific, warm North Atlantic) scenario. In contrast, in all cases, summer and fall

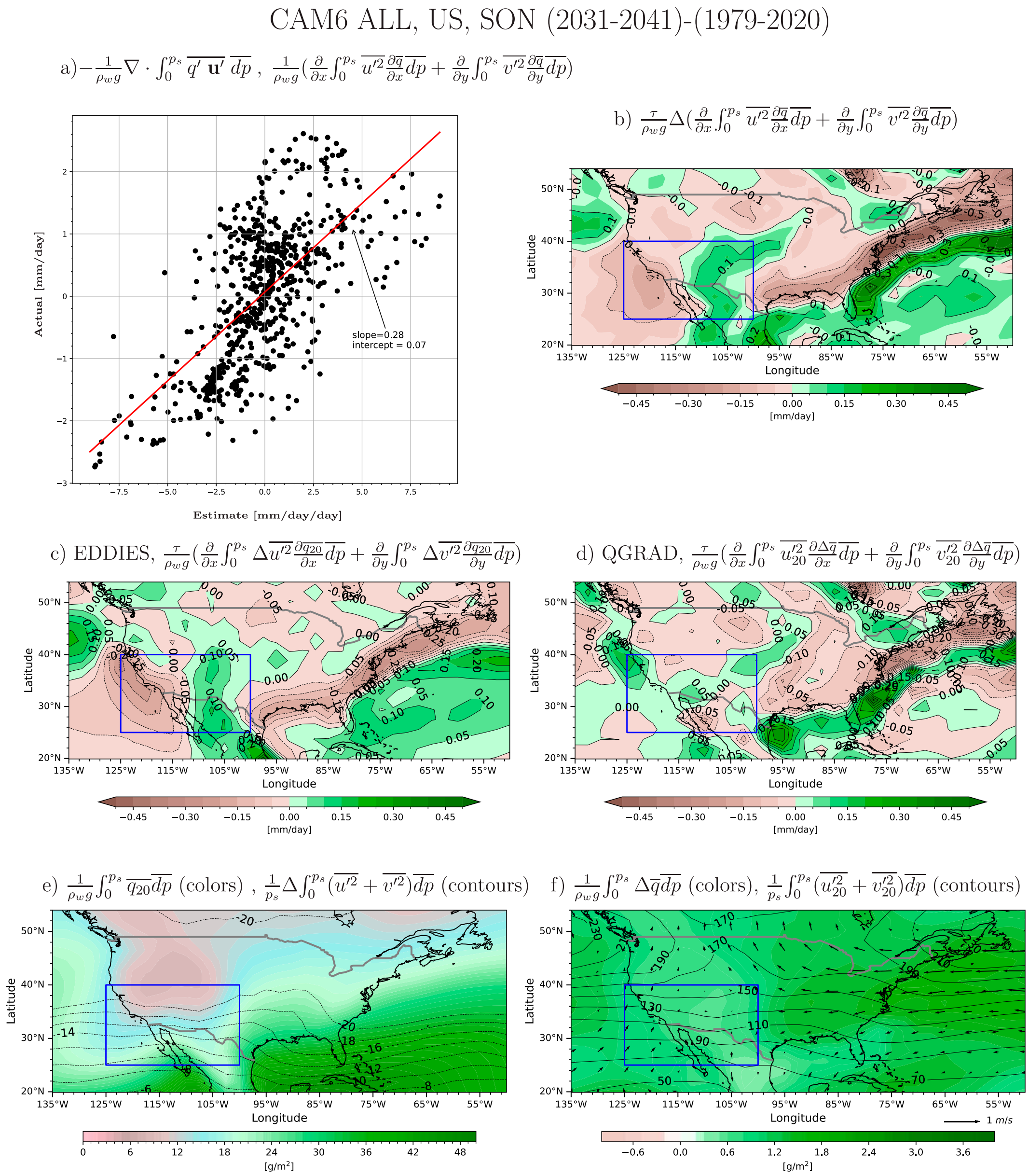

FIG. 10. The mixing length analysis of changes in transient eddy moisture flux convergence in SON. (a) The relation between actual and approximated transient eddy moisture convergence with the slope of the relation being an estimate of the time scale; (b) the change in mixing length estimated moisture convergence, the component of (b) due to changes in (c) eddies and (d) moisture gradients; (e) the climatological past vertically integrated humidity (colors) and change in vertically integrated eddy kinetic energy (contours); and (f) the change in vertically integrated moisture (colors) and past climatological vertically integrated transient eddy kinetic energy (contours) with change in 700-hPa winds as vectors. Units are millimeters per day for moisture divergence, grams per meter squared for vertically integrated moisture, and meters per second for winds with reference vector at lower right.

precipitation decreases, though by more in the worst-case ocean scenarios.

- In the best-case scenario with enhanced cool season precipitation, summer sm remains much as it was in the historical model simulation, while in the worst-case scenario and the average of all scenarios, it declines. Summer and fall precipitation decline across the grand ensemble, and fall sm is also universally reduced and, hence, these are radiatively forced. Fall drying sets the stage for winter soils that are either drier than the historical ensemble or, for the best-case scenarios, much as in the historical ensemble despite increased winter precipitation.
- In the best-case scenario, higher evapotranspiration in spring and summer offsets higher cool season precipitation and

prevents higher sm in summer. In the worst-case scenario, evapotranspiration is reduced year-round, which is also the case when averaging across the entire grand ensemble, though more weakly. In these cases, evapotranspiration is opposing the sm reduction driven by precipitation declines.

- In all but a few best-case scenarios, summer aridity goes along with a hydrological adjustment in which soils are drier but evapotranspiration and air humidity are reduced, while vapor pressure deficit increases.
- For the SWNA region as a whole, summer precipitation is reduced. In the worst-case and the average across all scenarios, summer precipitation decline is largely driven by a reduction in evapotranspiration and hence is a legacy of prior season reductions in precipitation. In the worst-case scenarios, the reduction in evapotranspiration is sufficiently strong that $P - \mathrm{ET}$ is positive and opposes the sm deficit. In contrast, for the best-case scenarios, increased cool season precipitation sustains increased evapotranspiration in summer which, along with reduced precipitation, generates negative $P - \mathrm{ET}$ that draws down sm.
- Across the scenarios, although SWNA dries as a region average, there is a region of summer precipitation increase in the northwest of SWNA. This is related to easterly anomalies equatorward of an anomalous high pressure ridge further north over North America. The easterly anomalies advect the higher climatological mean humidity from the plains and eastern United States into the southwest region.
- Precipitation declines in fall across the scenarios. This is caused by enhanced transient eddy moisture flux divergence. This arises from a combination of weaker eddies providing less transient eddy moisture flux convergence in the west of SWNA and also enhanced diffusion of moisture away from local maxima of humidity increases.

The work has, we believe, shed light on the mechanisms of ocean driving of the atmosphere and land–atmosphere coupling that lead to enhanced aridity, defined by reductions in sm, in southwest North America in the coming decades. We have drawn attention to the importance of precipitation, especially cool season precipitation, as a driver of summer sm. In the worst-case scenarios with reduced cool season precipitation, summer sm is strongly reduced, but in the best-case scenarios with increased cool season precipitation, it remains close to the historical values. During summer, sm drying cannot be thought of in terms of a warmer atmosphere increasing water vapor holding capacity and drawing more moisture from the soils. Instead, the cases with the driest soils have the largest reduction in evapotranspiration, the lowest atmospheric humidity, and the highest vapor pressure deficit. This hydrological arrangement is characteristic of sm control and is allowed for because the driest cases have the largest reduction of cool season precipitation. In addition, a transient eddy-driven drying of soils in fall, common to all scenarios and hence radiatively forced, is critical to ensure that, even in the best-case scenarios, winter soils are not much wetter than in the historical simulations despite increased winter precipitation. While the current work does not contradict much prior work on summer continental aridification, defined in terms of declining soil moisture, it does elucidate the mechanisms involved. Prior work could leave an impression that atmospheric warming increased evaporative demand and dries down soils by increased evapotranspiration. While this is seen to not be the cause in, for example, Cook et al. (2014), Berg et al. (2017), and Mankin et al. (2017), here we explain the important role prior season precipitation and evapotranspiration play in determining summer aridification. The important control of cool season precipitation on warm season tree growth in SWNA was also shown in Baek et al. (2017).

While this has been a mechanism study, it is important to note that in the majority of scenarios, the results project the continuation of intensifying aridity, as defined in terms of summer sm, in SWNA, and that even in the best-case scenario, a wetter climate is not reestablished. The drying is more severe if the recent trend toward an enhanced zonal SST gradient across the equatorial Pacific Ocean continues and is less severe if the cold tongue warms up as in CMIP6 models. Improved understanding adds confidence to these projections of further sm aridification of SWNA in the imminent future.

Of course, these results come from just one SST-forced climate model. However, these are the only model experiments that aim to directly assess how future climate will evolve under the influence of radiative forcing and plausible and realistic evolution of natural modes of decadal variability in the Pacific and Atlantic Oceans. This same modeling framework has been used to successfully simulate, as a response to changes in tropical SSTs, the spatial pattern and intensity of the pluvial to megadrought transition that occurred in southwest North America between the end of the twentieth century and beginning of the twenty-first century. Hence, we believe that the model experiments here provide realistic guidance on future southwest hydroclimate evolution under the influence of decadal variability. The lack of atmosphere–ocean coupling in the model setup did not obviously degrade those simulations, and SST-forced models have a long history of being used to explain ocean-driven climate variability (e.g., Lau and Nath 1994) even as problems arise from imposing extratropical SSTs that were in fact generated by the atmosphere (Barsugli and Battisti 1998; Bretherton and Battisti 2000). To address uncertainty in the forced SST change, the radiatively forced component includes two estimates: one observationally based and one CMIP6-based. However, the atmosphere response to them will be model dependent. To test that sensitivity, hopefully, in the future, similar experiments will be performed with other models.

As a caveat, much of the southwest North America study region is mountainous, and climate models such as used here do not have the resolution required to properly resolve the influence of topography on the atmosphere. Using higher-resolution model simulations would be attractive but computationally demanding to cover the comprehensive ranges of climate scenarios investigated here. Downscaling is an alternative but is challenging, including the limited in situ observational data at higher elevations (see Adhikari et al. 2024). Finally, it should always be noted that in the presence of $\mathrm{CO_2}$ rise with its physiological effects on vegetation, as well as an active role for plants in managing water, energy, and $\mathrm{CO_2}$ exchanges with the atmosphere, no simple extrapolation of sm drying to enhanced stress on vegetation is warranted (e.g., Berg and McColl 2021). Indeed, Earth system models project across wide swaths of land that vegetation health will increase due to the physiological effects of increased CO_2 even where soil moisture decreases and, in fact, the enhanced vegetation activity can actually reduce soil moisture (Mankin et al. 2017, 2018, 2019). Southwest North America is one such area though modeled increases in vegetation health are less striking than in other regions of the continent. Whether real-world vegetation will respond so positively as in models to rising CO_2 has been questioned based on the simplicity of modeling assumptions (see discussions in Cook et al. 2016, 2018; Berg and McColl 2021). Nonetheless, it would be worthwhile, but well beyond the scope of this study, to assess how these cross-season connections in the ocean–land–atmosphere system influence, and are influenced by, vegetation responses.

Acknowledgments. This work was supported by NOAA Award NA20OAR4310379 and NSF Awards AGS-2127684 and AGS-2101214. We thanks three reviewers for their useful comments and critiques.

Data availability statement. The model data used here are available at https://hodges.ldeo.columbia.edu:81/expert/SOURCES/.CAM6/.forRichard/.CAM6/.runs/. In that directory, *ensemble-extension-to-aug2021* contains the historical runs, and the projections are named according to the conventions for forcing and PDO and AMO combinations in the paper.

REFERENCES

Adhikari, P., B. Geerts, S. Rahimi-Esfarjani, K. Smith, B. N. Shuman, and T. L. Schneider, 2024: Evaluation of the mountain hydroclimate across the western United States in dynamically downscaled climate models. *J. Hydrometeor.*, **25**, 1877–1894, https://doi.org/10.1175/JHM-D-24-0063.1.

Baek, S. H., J. E. Smerdon, S. Coats, A. P. Williams, B. I. Cook, E. R. Cook, and R. Seager, 2017: Precipitation, temperature, and teleconnection signals across the combined North American, Monsoon Asia, and Old World Drought Atlases. *J. Climate*, **30**, 7141–7155, https://doi.org/10.1175/JCLI-D-16-0766.1.

Barsugli, J. J., and D. S. Battisti, 1998: The basic effects of atmosphere–ocean thermal coupling on midlatitude variability. *J. Atmos. Sci.*, **55**, 477–493, https://doi.org/10.1175/1520-0469(1998)055<0477:TBEOAO>2.0.CO;2.

Berg, A., and K. A. McColl, 2021: No projected global drylands expansion under greenhouse warming. *Nat. Climate Change*, **11**, 331–337, https://doi.org/10.1038/s41558-021-01007-8.

——, J. Sheffield, and P. C. D. Milly, 2017: Divergent surface and total soil moisture projections under global warming. *Geophys. Res. Lett.*, **44**, 236–244, https://doi.org/10.1002/2016GL071921.

Bretherton, C. S., and D. S. Battisti, 2000: An interpretation of the results from atmospheric general circulation models forced by the time history of the observed sea surface temperature distribution. *Geophys. Res. Lett.*, **27**, 767–770, https://doi.org/10.1029/1999GL010910.

Cook, B. I., J. E. Smerdon, R. Seager, and S. Coats, 2014: Global warming and 21st century drying. *Climate Dyn.*, **43**, 2607–2627, https://doi.org/10.1007/s00382-014-2075-y.

——, T. R. Ault, and J. E. Smerdon, 2015: Unprecedented 21st century drought risk in the American Southwest and Central Plains. *Sci. Adv.*, **1**, e1400082, https://doi.org/10.1126/sciadv.1400082.

——, E. R. Cook, J. E. Smerdon, R. Seager, A. P. Williams, S. Coats, D. W. Stahle, and J. Villaneuva Diaz, 2016: North American megadroughts in the Common Era: Reconstructions and simulations. *Wiley Interdiscip. Rev.: Climate Change*, **7**, 411–432, https://doi.org/10.1002/wcc.394.

——, J. S. Mankin, and K. J. Anchukaitis, 2018: Climate change and drought: From past to future. *Curr. Climate Change Rep.*, **4**, 164–179, https://doi.org/10.1007/s40641-018-0093-2.

——, ——, K. Marvel, A. P. Williams, J. E. Smerdon, and K. J. Anchukaitis, 2020: Twenty-first century drought projections in the CMIP6 forcing scenarios. *Earth's Future*, **8**, e2019EF001461, https://doi.org/10.1029/2019EF001461.

Danabasoglu, G., and Coauthors, 2020: The Community Earth System Model Version 2 (CESM2). *J. Adv. Model. Earth Syst.*, **12**, e2019MS001916, https://doi.org/10.1029/2019MS001916.

Greve, P., M. L. Roderick, A. M. Ukkola, and Y. Wada, 2019: The aridity index under global warming. *Environ. Res. Lett.*, **14**, 124006, https://doi.org/10.1088/1748-9326/ab5046.

Kushnir, Y., 1994: Interdecadal variations in North Atlantic Sea surface temperature and associated atmospheric conditions. *J. Climate*, **7**, 141–157, https://doi.org/10.1175/1520-0442(1994)007<0141:IVINAS>2.0.CO;2.

Lau, N.-C., and M. J. Nath, 1994: A modeling study of the relative roles of tropical and extratropical SST anomalies in the variability of the global atmosphere-ocean system. *J. Climate*, **7**, 1184–1207, https://doi.org/10.1175/1520-0442(1994)007<1184:AMSOTR>2.0.CO;2.

Lee, S., M. L'Heureux, A. T. Wittenberg, R. Seager, P. A. O'Gorman, and N. C. Johnson, 2022: On the future zonal contrasts of equatorial Pacific climate: Perspectives from observations, simulations, and theories. *npj Climate Atmos. Sci.*, **5**, 82, https://doi.org/10.1038/s41612-022-00301-2.

Lehner, F., C. Deser, N. Maher, J. Marotzke, E. M. Fischer, L. Brunner, R. Knutti, and E. Hawkins, 2020: Partitioning climate projection uncertainty with multiple large ensembles and CMIP5/6. *Earth Syst. Dyn.*, **11**, 491–508, https://doi.org/10.5194/esd-11-491-2020.

Li, C., and Coauthors, 2018: Midlatitude atmospheric circulation responses under 1.5 and 2.0°C warming and implications for regional impacts. *Earth Syst. Dyn.*, **9**, 359–382, https://doi.org/10.5194/esd-9-359-2018.

Lickley, M., and S. Solomon, 2018: Drivers, timing and some impacts of global aridity change. *Environ. Res. Lett.*, **13**, 104010, https://doi.org/10.1088/1748-9326%2Faae013.

Maloney, E. D., and Coauthors, 2014: North American climate in CMIP5 experiments: Part III: Assessment of twenty-first-century projections. *J. Climate*, **27**, 2230–2270, https://doi.org/10.1175/JCLI-D-13-00273.1.

Manabe, S., R. T. Wetherald, and R. J. Stouffer, 1981: Summer dryness due to an increase of atmospheric CO_2 concentration. *Climatic Change*, **3**, 347–386, https://doi.org/10.1007/BF02423242.

Mankin, J. S., J. E. Smerdon, B. I. Cook, A. P. Williams, and R. Seager, 2017: The curious case of projected twenty-first-century drying but greening in the American West. *J. Climate*, **30**, 8689–8710, https://doi.org/10.1175/JCLI-D-17-0213.1.

——, R. Seager, J. E. Smerdon, B. I. Cook, A. P. Williams, and R. M. Horton, 2018: Blue water trade-offs with vegetation in a CO_2-enriched climate. *Geophys. Res. Lett.*, **45**, 3115–3125, https://doi.org/10.1002/2018GL077051.

——, ——, ——, ——, and ——, 2019: Mid-latitude freshwater availability reduced by projected vegetation responses to climate change. *Nat. Geosci.*, **12**, 983–988, https://doi.org/10.1038/s41561-019-0480-x.

Milly, P. C. D., and K. A. Dunne, 2011: On the hydrologic adjustment of climate-model projections: The potential pitfall of potential evapotranspiration. *Earth Interact.*, **15**, 1–14, https://doi.org/10.1175/2010EI363.1.

——, and ——, 2016: Potential evapotranspiration and continental drying. *Nat. Climate Change*, **6**, 946–949, https://doi.org/10.1038/nclimate3046.

Newman, M., and Coauthors, 2016: The Pacific decadal oscillation, revisited. *J. Climate*, **29**, 4399–4427, https://doi.org/10.1175/JCLI-D-15-0508.1.

Scheff, J., and D. M. W. Frierson, 2014: Scaling potential evapotranspiration with greenhouse warming. *J. Climate*, **27**, 1539–1558, https://doi.org/10.1175/JCLI-D-13-00233.1.

——, and ——, 2015: Terrestrial aridity and its response to greenhouse warming across CMIP5 climate models. *J. Climate*, **28**, 5583–5600, https://doi.org/10.1175/JCLI-D-14-00480.1.

Seager, R., and N. Henderson, 2013: Diagnostic computation of moisture budgets in the ERA-interim reanalysis with reference to analysis of CMIP-archived atmospheric model data. *J. Climate*, **26**, 7876–7901, https://doi.org/10.1175/JCLI-D-13-00018.1.

——, N. Naik, and L. Vogel, 2012: Does global warming cause intensified interannual hydroclimate variability? *J. Climate*, **25**, 3355–3372, https://doi.org/10.1175/JCLI-D-11-00363.1.

——, H. Liu, N. Henderson, I. Simpson, C. Kelley, T. Shaw, Y. Kushnir, and M. Ting, 2014a: Causes of increasing aridification of the Mediterranean region in response to rising greenhouse gases. *J. Climate*, **27**, 4655–4676, https://doi.org/10.1175/JCLI-D-13-00446.1.

——, and Coauthors, 2014b: Dynamical and thermodynamical causes of large-scale changes in the hydrological cycle over North America in response to global warming. *J. Climate*, **27**, 7921–7948, https://doi.org/10.1175/JCLI-D-14-00153.1.

——, M. Ting, P. Alexander, J. Nakamura, H. Liu, C. Li, and M. Newman, 2023: Ocean-forcing of cool season precipitation drives ongoing and future decadal drought in southwestern North America. *npj Climate Atmos. Sci.*, **6**, 141, https://doi.org/10.1038/s41612-023-00461-9.

Swann, A. L. S., F. M. Hoffman, C. D. Koven, and J. T. Randerson, 2016: Plant responses to increasing CO_2 reduce estimates of climate impacts on drought severity. *Proc. Natl. Acad. Sci. USA*, **113**, 10 019–10 024, https://doi.org/10.1073/pnas.1604581113.

Ting, M., R. Seager, C. Li, H. Liu, and N. Henderson, 2021: Future summer drying in the U.S. Corn Belt and the role of midlatitude storm tracks. *J. Climate*, **34**, 9043–9056, https://doi.org/10.1175/JCLI-D-20-1004.1.

Tuel, A., and E. A. B. Eltahir, 2021: Mechanisms of European summer drying under climate change. *J. Climate*, **34**, 8913–8931, https://doi.org/10.1175/JCLI-D-20-0968.1.

Vicente-Serrano, S. M., D. Peña-Angulo, S. Beguería, F. Domínguez-Castro, M. Tomás-Burguera, I. Noguera, L. Gimeno-Sotelo, and A. El Kenawy, 2022: Global drought trends and future projections. *Philos. Trans. Roy. Soc.*, **A380**, 20210285, https://doi.org/10.1098/rsta.2021.0285.

Williams, A. P., and Coauthors, 2020: Large contribution from anthropogenic warming to an emerging North American megadrought. *Science*, **368**, 314–318, https://doi.org/10.1126/science.aaz9600.

——, B. I. Cook, and J. E. Smerdon, 2022: Rapid intensification of the emerging southwestern North American megadrought in 2020–2021. *Nat. Climate Change*, **12**, 232–234, https://doi.org/10.1038/s41558-022-01290-z.